

中国激光

1064 nm 光纤激光器直写聚酰亚胺成碳工艺参数研究

王进¹, 周如东³, 张宁⁴, 成骏峰¹, 曹峰¹, 王强¹, 吴盾^{1,5*}*, 刘春林^{1,2*}

¹常州大学材料科学与工程学院, 江苏省环境友好高分子材料重点实验室, 江苏 常州 213164;

²常州大学怀德学院, 江苏 靖江 214500;

³中海油常州涂料化工研究院有限公司, 江苏 常州 213016;

⁴常州工业职业技术学院, 江苏 常州 213164;

⁵材料科学与工程国家级实验教学示范中心, 江苏 常州 213164

摘要 采用波长为 1064 nm 的光纤激光器对聚酰亚胺(PI)膜进行激光碳化工艺试验, 研究了激光线间距与光斑直径、扫描速度与脉冲频率、激光功率对激光直写 PI 膜成碳性能的影响规律。结果表明: 激光直写 PI 膜的产物为三维多孔碳层结构, 其中, C、N、O 元素的质量分数分别为 84.84%、2.02%、13.14%; 激光线间距与光斑直径、扫描速度与脉冲频率、激光功率这三组工艺参数均会不同程度地影响激光直写 PI 膜的成碳性能; 通过研究激光直写 PI 膜成碳的导电性能得到了最佳工艺参数: 激光线间距为 0.001 mm, 光斑直径为 0.06 mm, 扫描速度为 150 mm/s, 脉冲频率为 40 kHz, 激光功率为 2.2 W; 在该工艺参数下, 激光直写 PI 膜的成碳缺陷比例最低, 其碳层的方块电阻可低至 55 Ω/sq。

关键词 激光技术; 激光直写; 聚酰亚胺; 工艺参数; 成碳性能

中图分类号 O633.4

文献标志码 A

doi: 10.3788/CJL202148.1002112

1 引言

石墨烯是一种由单层碳原子紧密堆积而成的具有蜂窝状结构的二维材料, 得益于其独特的晶体结构和电子结构, 石墨烯有着出众的物理化学性质^[1-2]。这些独特的物理化学性质使石墨烯在电子信息^[3-4]、能量存储^[5-6]、柔性显示^[7-8]、复合材料制备^[9-10]、生物和仿生^[11-12]等方面具有广阔的应用前景。合成石墨烯的前驱体处理方法有两种: 一种是化学还原法, 另一种是热处理法^[13-16]。传统的石墨烯生产方法不仅工艺繁杂, 而且对设备的要求比较严苛, 导致能源浪费现象比较突出; 与此同时, 强毒性或高温环境等加工条件对生产设备提出了较高的使用和安全标准。因此, 急切需要一种既不依赖使用高毒性化工试剂, 又不需要特殊高温处理的替代方法, 且最好能够实现“一步法”制备石墨烯。

激光加工技术是一种高效的加工制造手段, 该技术可以在材料上实现表面处理和微加工, 已被广泛应用于加工制造工艺领域^[17-18]。2014 年, 美国莱斯大学 James M. Tour 团队^[19]首次报道了使用 CO₂ 激光器在商业聚酰亚胺(PI)膜表面进行激光直写, 采用“一步法”制备了少层多孔激光诱导石墨烯(LIG)片。与二维石墨烯单晶相比, 这种三维多孔石墨烯具有很多独特的物理化学性质, 为众多领域中石墨烯器件的发展提供了新思路。另外, Wang 等^[20]使用波长为 455 nm、输出功率为 5 W 的蓝光激光器直写 PI 膜也成功制备出了石墨烯, 并证明了激光制备石墨烯取决于输出功率, 而与激光的波长无关。2018 年, Duy 等^[21]通过实验发现, 激光制备石墨烯的临界能量密度约为 5.5 J·cm⁻², 过低的能量密度会导致 PI 膜的石墨化程度不足。Chyan 等^[22]提出了一种使用多次脉冲激光划线将衬底转

收稿日期: 2020-10-09; 修回日期: 2020-11-16; 录用日期: 2020-11-23

基金项目: 江苏省第十五批“六大人才高峰”创新人才团队项目(TD-XCL-026)、江苏省环境友好高分子材料重点实验室开放课题(PML1803)

*E-mail: chunlin@cczu.edu.cn; **E-mail: 1348260409@qq.com

变成激光诱导石墨烯的方法,可应用该方法的衬底材料种类繁多:从可再生材料(如食物、布料等)到高性能聚合物,甚至可以是天然煤炭。

目前,国内关于激光直写PI膜的相关研究较少,还没有人通过系统的研究来探索激光工艺参数对激光直写PI膜成碳性能的影响。激光直写PI膜技术不仅可以实现石墨烯的快速生产,而且不需要传统石墨烯制备方法中的严苛条件。鉴于此,本文深入研究了各种激光工艺参数对激光直写PI膜成碳性能的影响,为优化激光直写PI膜成碳工艺提供参考依据。

2 实验部分

2.1 实验材料

PI膜,购于上海特翔电器绝缘材料有限公司;无水乙醇(分析纯),购于国药集团化学试剂有限公司;去离子水,自制。

2.2 样品制备

激光直写PI膜成碳过程如图1所示。PI膜吸收1064 nm激光的能量,产生瞬时高温,PI分子链在高温下发生化学键的断裂和重排^[23],激光直写区域由棕黄色变成黑色。在本实验中,激光直写PI膜采用的是FMF20W脉冲光纤激光器,其最大输出功率为20 W,波长为1064 nm,最高脉冲频率为90 kHz。采用振镜扫描激光头,以实现对激光光斑运动轨迹的精确控制。为保证激光直写线路的连续性和稳定性,本文实验均选用S形激光走线的扫描方式。在激光直写PI膜之前,先用去离子水和无水乙醇对250 μm厚的PI膜表面进行清洗,以去除其表面的灰尘等;然后将PI膜置于50 °C的干燥箱中干燥8 h;最后,将PI膜平整地固定在操作台上,调整光纤激光器的焦点与PI膜的表面重合,设置激光加工工艺参数和扫描路径后,通过计算机操控激光器进行直写。本实验中的激光直写图形设计为长30 mm、宽5 mm的矩形结构。

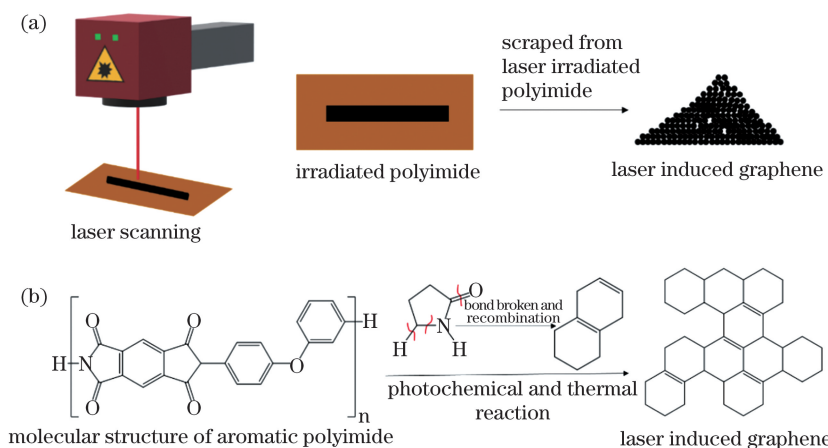


图1 激光直写PI膜成碳。(a)工艺示意图;(b)原理示意图

Fig. 1 Carbon formation by laser direct writing PI film. (a) Process diagram; (b) principle diagram

2.3 测试与表征

采用SUPRA55型场发射扫描电镜(SEM)观察激光直写PI膜产物的微观形貌;采用DXR2型激光共聚焦拉曼光谱仪对激光直写PI膜表面的碳化程度进行表征;采用Mg K α 激发源(1253.6 eV)的VG ESCALab MK II X射线光电子能谱仪记录激光直写PI膜产物的X射线光电子能谱(XPS),所有结合能都参考284.5 eV处的C1s峰进行计算,用各元素的峰面积比较正、计算元素的组成;采用RTS-8型四探针测量仪测量激光直写PI膜产物的表面方块电阻;采用JC200D型静态接触角测量仪测试激光直写PI膜产物的表面接触角。

3 结果与讨论

3.1 激光直写PI膜成碳分析

3.1.1 激光直写PI膜产物的微观形貌分析

图2为激光直写PI膜产物表面和截面的扫描电镜分析结果。从图2(a)中可以看到,激光直写PI膜产物是由众多不规则的絮状碳颗粒组成的一个连续多孔的立体结构。这种结构的形成可能与激光直写材料的表面有关。激光快速照射产生瞬间高温高压,材料表面的有机物分解,热解产生的气体快速逸出,从而造就了特定的形貌。根据图2(b)中激光直写PI膜产物的截面形貌可知,PI膜并没有被激光

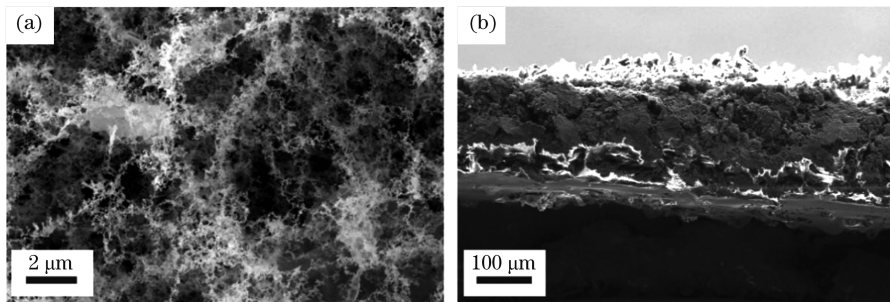


图2 激光直写PI膜产物的微观形貌。(a)表面形貌;(b)截面形貌

Fig. 2 Micro morphologies of product formed by laser direct writing PI film. (a) Surface morphology; (b) cross-section morphology

完全烧蚀,其表面出现了许多“站立”的絮状物,内部的碳层存在很多大小不一的孔洞,残留的PI膜为材料提供了有效的力学强度。

3.1.2 激光直写前后PI膜的拉曼光谱分析

激光直写后PI膜表面发生碳化,为了进一步表征激光直写后表面碳层的石墨化程度,使用拉曼光谱仪对样品进行分析。图3为激光直写前后PI膜表面碳颗粒的拉曼光谱,可以清楚地看到,原PI膜的特征峰在激光直写后被碳的三个特征峰取代,分

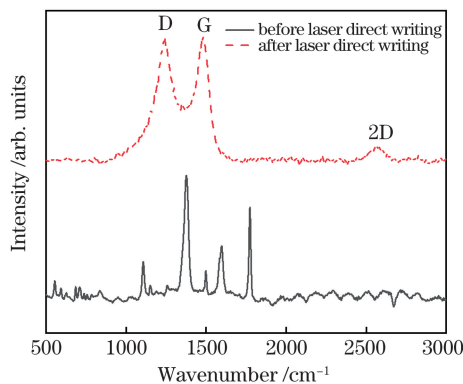


图3 激光直写前后PI膜的拉曼光谱图

Fig. 3 Raman spectra of PI film before and after laser direct writing

别为 1344 cm^{-1} 和 1500 cm^{-1} 附近的D峰和G峰,以及 2683 cm^{-1} 附近的2D峰,且D峰的强度低于G峰。这一结果说明激光直写后PI膜形成了碳结构,石墨化程度较高。

3.1.3 激光直写PI膜产物的XPS分析

图4为激光直写PI膜产物的XPS分析结果。由图4(a)中的结合能全谱图可知,激光直写PI膜产物的XPS谱图中显示只有C1s、O1s、N1s峰。其中,N1s代表测试样品材料中含有氮元素,O1s代表材料表面含有含氧官能团。由各个峰面积之比可以计算出激光直写PI膜产物中C、N、O元素的质量分数分别为84.84%、2.02%、13.14%。图4(b)为激光直写PI膜产物的高分辨C1s XPS谱图,碳原子以C—C、C—O—C、C—N和C=O四种形态存在,其中C—C为激光直写PI膜产物中碳元素的主要成分。

3.2 工艺参数对激光直写PI膜产物性能的影响

3.2.1 激光线间距与光斑直径对激光直写PI膜产物导电性能的影响

在激光功率为2.4 W、扫描速度为120 mm/s、脉冲频率为36 kHz的条件下研究激光线间距(0.001~0.010 mm)与光斑直径(d (0.03~0.07 mm)

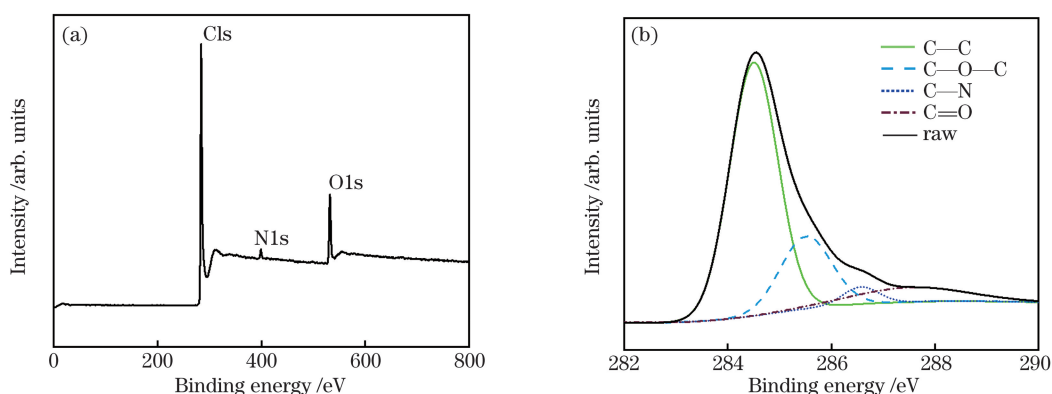


图4 激光直写PI膜产物的XPS谱图。(a)XPS结合能全谱图;(b)高分辨C1s XPS谱图

Fig. 4 XPS spectra of product formed by laser direct writing PI film. (a) XPS binding energy full spectrum; (b) high resolution C1s XPS spectrum

对激光直写 PI 膜产物导电性能的影响,实验结果如表 1 和图 5 所示。可以看出:在相同的线间距下,随着光斑增大,激光直写 PI 膜产物的方块电阻先降低后增大。在相同的线间距下,当光斑太小时,相邻两条线之间的重叠区域小,使得相同区域被重复照射的次数较少,PI 膜的碳化程度太低,方块电阻很大;

表 1 不同线间距和光斑直径下激光直写 PI 膜产物的方块电阻

Table 1 Sheet resistance of product formed by laser direct writing PI film under different line spacing and spot diameter values

Line spacing /mm	Sheet resistance /($\Omega \cdot \text{sq}^{-1}$)				
	$d = 0.03 \text{ mm}$	$d = 0.04 \text{ mm}$	$d = 0.05 \text{ mm}$	$d = 0.06 \text{ mm}$	$d = 0.07 \text{ mm}$
0.001	102	70	67	62	123
0.002	101	120	102	85	105
0.003	277	321	123	184	240
0.005	392	591	262	345	435
0.007	1315	2446	692	571	2608
0.010	14753	12339	6731	5973	8568

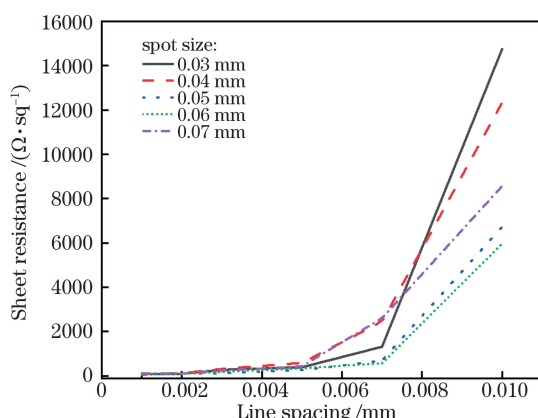


图 5 不同线间距和光斑直径下激光直写 PI 膜产物的方块电阻

Fig. 5 Sheet resistance of product formed by laser direct writing PI film under different line spacing and spot diameter values

3.2.2 脉冲频率与扫描速度对激光直写 PI 膜产物导电性能的影响

在激光功率为 2.4 W、光斑直径为 0.06 mm、线间距为 0.001 mm 的条件下,研究激光扫描速度(100~300 mm/s)和脉冲频率 f (30~55 kHz)对激光直写 PI 膜产物导电性能的影响,实验结果如表 2 和图 6 所示。当扫描速度为 100 mm/s 时,随着脉冲频率的增加,激光直写 PI 膜产物的方块电阻越来越大。此时的扫描速度太慢,导致激光照射的点与点之间的距离太近,重叠区域太大,随着脉冲频率增

随着光斑的增大,相邻两条线之间的重叠区域增大,PI 膜被激光重复照射的次数增多,增大了 PI 膜的碳化程度,方块电阻降低;随着光斑继续增大,激光重复照射的次数过多,形成的碳层被破坏和烧蚀,方块电阻变大。在相同的光斑下,激光直写 PI 膜产物的方块电阻基本随着线间距的减小呈降低的趋势。

加发生了类似于激光切割的情况,最终的结果是激光击穿材料表面。在扫描速度为 150 mm/s 和 200 mm/s 时,随着脉冲频率的增加,激光直写 PI 膜产物的方块电阻先降低而增加。脉冲频率太低时,相邻两点之间的重叠区域小,相同位置的照射次数不够,PI 膜的碳化程度低,方块电阻较大;随着脉冲频率的增加,相邻两点之间的连续性逐渐增加,方块电阻降低;随着脉冲频率继续增加,相同位置被重复照射的次数过多,碳层被破坏,因此方块电阻增大。当扫描速度为 250 mm/s 和 300 mm/s 时,随着脉冲频率的增加,激光直写 PI 膜产物的方块电阻呈下降趋势。此时的激光扫描速度太快,导致相邻两点之间的距离太远,脉冲频率的增加减小了相邻两点之间的距离,PI 膜成碳的连续性更好,导电性能增加。

3.2.3 激光功率对激光直写 PI 膜成碳性能的影响

为研究激光功率对激光直写 PI 膜成碳性能的影响,在光斑直径为 0.06 mm、线间距为 0.001 mm、扫描速度为 150 mm/s、脉冲频率为 40 kHz 的条件下,选取激光功率为 1.8~2.8 W 进行激光直写实验。

1) 对激光直写 PI 膜产物形貌的影响

利用扫描电子显微镜观察不同激光功率作用下激光直写 PI 膜产物的表面形貌,可以看出,随着激光功率增加,PI 膜的表面损伤程度逐渐增大。由图 7(a)、(b)可以看出,激光直写后只在 PI 膜表面

表2 不同扫描速度和脉冲频率下激光直写PI膜产物的方块电阻

Table 2 Sheet resistance of product formed by laser direct writing PI film under different scanning speeds and pulse frequencies

Scanning speed / (mm·s ⁻¹)	Sheet resistance /($\Omega \cdot \text{sq}^{-1}$)					
	f=30 kHz	f=35 kHz	f=40 kHz	f=45 kHz	f=50 kHz	f=55 kHz
100	1419	1614	1750	3932		
150	110	73	61	69	73	215
200	146	96	81	72	69	74
250	159	103	88	76	72	68
300	267	155	112	95	85	83

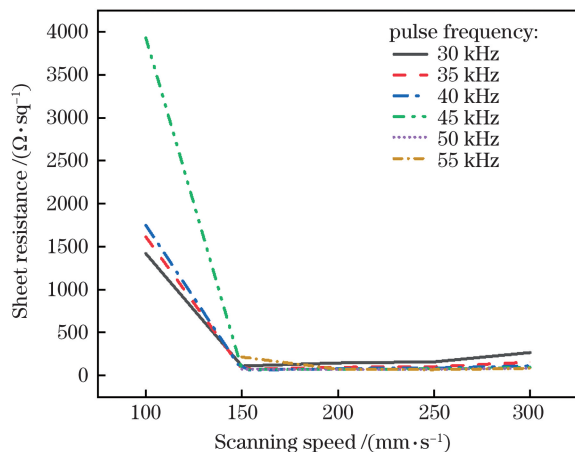


图6 不同扫描速度和脉冲频率下激光直写PI膜产物的方块电阻

Fig. 6 Sheet resistance of product formed by laser direct writing PI film under different scanning speeds and pulse frequencies

留下了一些絮状碳颗粒,保留了原PI膜的平整性,且图7(b)中的絮状碳颗粒有所增多,表面上出现了一些褶皱。图7(c)、(d)中的絮状结构开始聚集成片,且图7(d)中的絮状结构进一步增多,覆盖在原PI膜上。由图7(e)、(f)可以看出,激光彻底破坏了原来的表面,表面的絮状结构和内部的碳颗粒形成了三维多孔结构,其形成的原因可能是激光快速照射过程中产生了瞬间高温高压,氧和氮键断裂,这些氮和氧原子在键断裂后转化为相应的气体,并从衬底逃逸。微观形貌的改变对激光直写PI膜产物的导电性能和亲疏水性等有很大影响。

2) 对激光直写PI膜产物拉曼光谱的影响

石墨类材料的拉曼光谱主要包含G峰、D峰以及2D峰。G峰是石墨类材料的主要特征峰,是由sp²碳原子的面内振动引起的,它通常出现在1580 cm⁻¹附近,该峰能有效反映石墨类材料的规整程度。D峰是由晶格振动离开布里渊区中心引起

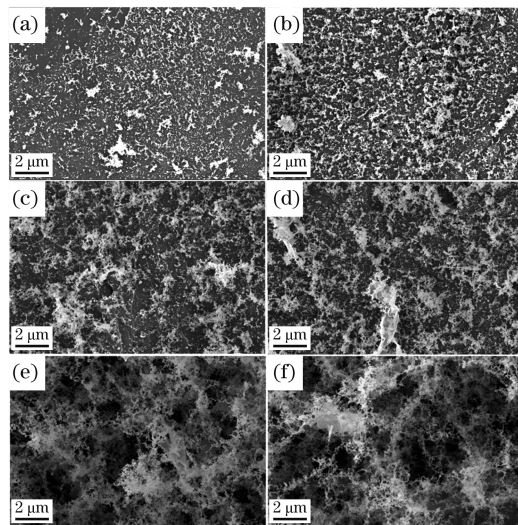


图7 不同激光功率下激光直写PI膜产物表面的扫描电镜图像。(a) 1.8 W; (b) 2.0 W; (c) 2.2 W; (d) 2.4 W; (e) 2.6 W; (f) 2.8 W

Fig. 7 SEM images of product formed by laser direct writing PI film under different laser powers.
(a) 1.8 W; (b) 2.0 W; (c) 2.2 W; (d) 2.4 W;
(e) 2.6 W; (f) 2.8 W

的,该峰通常会出现在1350 cm⁻¹附近,用于表征石墨类材料样品的结构缺陷或边缘,被认为是石墨类材料的无序振动峰。一般用D峰与G峰的强度比(I_D/I_G)来表征石墨类材料中的缺陷密度^[24]。2D峰是双声子共振二阶拉曼峰,通常出现在2700 cm⁻¹附近,与石墨类材料样品中碳原子层的层数有关。一般用2D峰与G峰的强度比(I_{2D}/I_G)来表征石墨烯类材料的堆叠层数^[25]。

如图8(a)、(b)所示,可以通过比较D峰、2D峰和G峰相对强度的比值(I_D/I_G 和 I_{2D}/I_G)来分析激光功率对激光直写PI膜成碳质量的影响: I_D/I_G 的值越小,说明碳材料的缺陷越少; I_{2D}/I_G 的值越大,说明碳层堆叠的层数越多。随着激光功率从1.8 W增加到2.8 W,2D峰的峰值强度呈现先上升

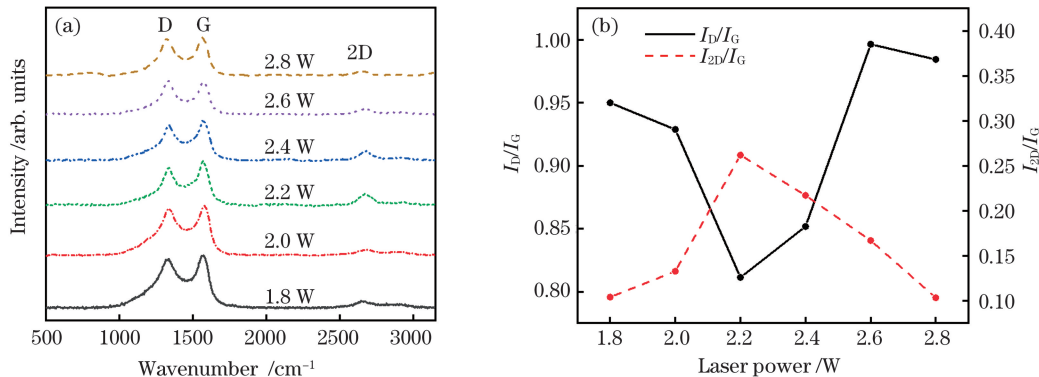


图8 不同激光功率下激光直写PI膜产物的拉曼光谱及拉曼峰强比。(a)拉曼光谱;(b)拉曼峰强比

Fig. 8 Raman spectra and Raman peak intensity ratio of product formed by laser direct writing PI film under different laser powers. (a) Raman spectra; (b) Raman peak intensity ratio

后下降的趋势，并在 2.2 W 处达到最大值；与此相反，D 峰的峰值强度呈现先下降后上升的趋势，并在 2.2 W 处达到最小值。这一结果表明，在 2.2 W 处，激光直写 PI 膜产物的成碳缺陷比例最低并且碳结晶率最高。

3) 对激光直写 PI 膜产物导电性能的影响

从图 9 中可以看出，激光直写 PI 膜产物的方块电阻随着激光功率的增加呈现出先减小后增大的趋

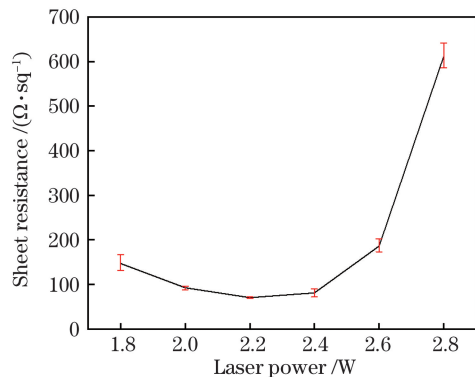


图9 激光功率对激光直写PI膜产物导电性能的影响

Fig. 9 Influence of laser power on conductivity of product formed by laser direct writing PI film

势。激光照射材料表面时，能量聚集在材料表面，PI 膜快速碳化；随着激光功率增大，激光烧蚀的深度越来越大，形成的碳颗粒之间的连续性增强。当激光功率为 2.2 W 时，激光直写 PI 膜产物的方块电阻低至 55 Ω/sq ，但是随着激光功率的进一步增加，碳层表面被激光烧蚀，部分碳颗粒在激光冲击下脱离碳层到周围环境中，碳层的连续性受到破坏，方块电阻变大。

4) 对激光直写 PI 膜产物表面接触角的影响

图 10 给出了激光直写 PI 膜产物表面接触角的变化。从图中可以看出：接触角随着激光功率的增加而增大。当激光功率为 1.8 W 和 2.0 W 时，因激光功率太低，激光直写 PI 膜产物的表面粗糙度并没发生明显变化，接触角与原 PI 膜表面接触角相差不大；随着激光功率增加，当激光功率为 2.2 W 和 2.4 W 时，激光直写 PI 膜产物表面出现了絮状结构，表面粗糙度增加，接触角变大，表现出一定的疏水性能；随着激光功率继续增大，高的激光功率使 PI 膜的表面和内部均被碳化，形成了粗糙度很大的三维多孔结构，接触角进一步增大，表现出超疏水性能。

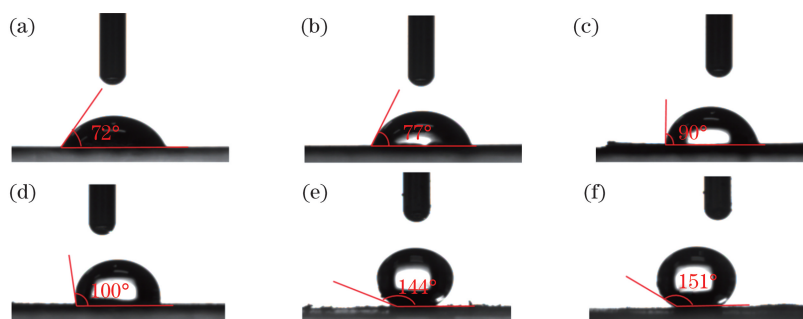


图10 激光功率对激光直写PI膜产物表面接触角的影响。(a) 1.8 W;(b) 2.0 W;(c) 2.2 W;(d) 2.4 W;(e) 2.6 W;(f) 2.8 W

Fig. 10 Influence of laser power on the contact angle of product formed by laser direct writing PI film. (a) 1.8 W; (b) 2.0 W; (c) 2.2 W; (d) 2.4 W; (e) 2.6 W; (f) 2.8 W

4 结 论

本文通过激光直写PI膜成碳实验,研究了激光线间距与光斑直径、扫描速度与脉冲频率、激光功率对PI膜成碳的影响,分析了激光直写PI膜产物的方块电阻,并详细分析了激光功率对激光直写PI膜产物微观形貌、成碳质量和亲疏水性的影响。得到以下主要结论:

1) 在脉冲激光作用下,PI膜吸收激光能量,进行光热转化,形成了连续多孔的三维立体碳层结构,PI分子链中发生了C—H、C=O、C—N等化学键的断裂和重排;激光直写PI膜产物中C、N、O元素的质量分数分别为84.84%、2.02%、13.14%。

2) 光纤激光器激光直写PI膜产物导电性能最佳的参数条件为:激光线间距0.001 mm,光斑直径0.06 mm,扫描速度150 mm/s,脉冲频率40 kHz。

3) 随着激光功率增大,激光直写PI膜被烧蚀的程度逐渐增大,其表面从少量的絮状碳颗粒变成三维多孔碳结构;由 I_D/I_G 值和 I_{2D}/I_G 值可知:碳层的缺陷程度先降低后增大,且在激光功率为2.2 W时最低,此时,方块电阻也最小,为55 Ω/sq。另外,激光直写PI膜产物的水接触角随着激光功率的增加而逐渐增大,在激光功率为2.8 W时,表现出了超疏水性。

参 考 文 献

- [1] Wang X X, Cao M S. Low-dimensional electromagnetic functional materials [J]. Surface Technology, 2020, 49(2): 18-28, 40.
王希晰, 曹茂盛. 特色研究报告:低维电磁功能材料研究进展[J]. 表面技术, 2020, 49(2): 18-28, 40.
- [2] Ye X K, Zhou Q L, Wan Z Q, et al. Research progress in electrode materials and devices of flexible supercapacitors [J]. Chemistry, 2017, 80(1): 10-33, 76.
叶星柯, 周乾隆, 万中全, 等. 柔性超级电容器电极材料与器件研究进展[J]. 化学通报, 2017, 80(1): 10-33, 76.
- [3] Zhou Y X, Huang Y Y, Jin Y P, et al. Terahertz properties of graphene and graphene-based terahertz devices [J]. Chinese Journal of Lasers, 2019, 46(6): 0614011.
周译玄, 黄媛媛, 靳延平, 等. 石墨烯太赫兹波段性质及石墨烯基太赫兹器件[J]. 中国激光, 2019, 46(6): 0614011.
- [4] Wu J J, Zhao H X, Gao J X, et al. Enhancing light absorption of graphene using magneto-optical photonic crystals [J]. Chinese Journal of Lasers, 2020, 47(4): 0403003.
武继江, 赵浩旭, 高金霞, 等. 基于磁光光子晶体的石墨烯光吸收增强[J]. 中国激光, 2020, 47(4): 0403003.
- [5] Aradilla D, Delaunay M, Sadki S, et al. Vertically aligned graphene nanosheets on silicon using an ionic liquid electrolyte: towards high performance on-chip micro-supercapacitors [J]. Journal of Materials Chemistry A, 2015, 3(38): 19254-19262.
- [6] Wu Z S, Parvez K, Feng X, et al. Graphene-based in-plane micro-supercapacitors with high power and energy densities [J]. Nature Communications, 2013, 4: 2487.
- [7] Kim H J, Kim Y J. Influence of external forces on the mechanical characteristics of the α-IGZO and graphene based flexible display [J]. IOP Conference Series: Materials Science and Engineering, 2014, 62: 012022.
- [8] Wang J, Liang M H, Fang Y, et al. Rod-coating: towards large-area fabrication of uniform reduced graphene oxide films for flexible touch screens [J]. Advanced Materials, 2012, 24(21): 2874-2878.
- [9] Kundu D P, Krumeich F, Nesper R, et al. Investigation of nano-fibrous selenium and its polypyrrole and graphene composite as cathode material for rechargeable Li-batteries [J]. Journal of Power Sources, 2013, 236: 112-117.
- [10] Li C Z, Wang Z B, Sui X L, et al. Ultrathin graphitic carbon nitride nanosheets and graphene composite material as high-performance PtRu catalyst support for methanol electro-oxidation [J]. Carbon, 2015, 93: 105-115.
- [11] Ji M Y, Jiang N, Chang J, et al. Near-infrared light-driven, highly efficient bilayer actuators based on polydopamine-modified reduced graphene oxide [J]. Advanced Functional Materials, 2014, 24(34): 5412-5419.
- [12] Zhang H Q, Sun L X, Yang Y Z, et al. Graphene-based optical biosensor using functionalized magnetic nanoparticles [J]. Acta Optica Sinica, 2020, 40(11): 1117001.
张慧琴, 孙立勋, 杨艺哲, 等. 一种基于功能化修饰磁性纳米颗粒的石墨烯基光学生物传感器[J]. 光学学报, 2020, 40(11): 1117001.
- [13] Larciprete R, Fabris S, Sun T, et al. Dual path mechanism in the thermal reduction of graphene oxide [J]. Journal of the American Chemical Society, 2011, 133(43): 17315-17321.
- [14] Moon I K, Lee J, Lee H, et al. Highly qualified reduced graphene oxides: the best chemical reduction

- [J]. Chemical Communications, 2011, 47 (34): 9681-9683.
- [15] Gao X F, Jang J, Nagase S, et al. Hydrazine and thermal reduction of graphene oxide: reaction mechanisms, product structures, and reaction design [J]. The Journal of Physical Chemistry C, 2010, 114 (2): 832-842.
- [16] Yan R S, Yao J M, Jia L X, et al. Progress in the research on structures and performances of functional graphene composite fibers [J]. Textile Auxiliaries, 2017, 34(11): 5-10.
阎若思, 姚继明, 贾立霞, 等. 石墨烯功能复合纤维的结构与性能研究进展 [J]. 印染助剂, 2017, 34 (11): 5-10.
- [17] Cheng J, Liu C S, Shang S, et al. A review of ultrafast laser materials micromachining [J]. Optics & Laser Technology, 2013, 46: 88-102.
- [18] Qi N J, Yuan X D, Zhang L J, et al. Three-dimensional detection technology of laser damage residual stress [J]. Chinese Journal of Lasers, 2020, 47(10): 1004001.
齐乃杰, 袁晓东, 张丽娟, 等. 激光损伤残余应力三维检测技术 [J]. 中国激光, 2020, 47(10): 1004001.
- [19] Lin J, Peng Z, Liu Y, et al. Laser-induced porous graphene films from commercial polymers [J]. Nature Communications, 2014, 5: 5714.
- [20] Wang Z Y, Wang G C, Liu W G, et al. Patterned laser-induced graphene for terahertz wave modulation [J]. JOSA B, 2020, 37(2): 546-551.
- [21] Duy L X, Peng Z W, Li Y L, et al. Laser-induced graphene fibers [J]. Carbon, 2018, 126: 472-479.
- [22] Chyan Y, Ye R Q, Li Y L, et al. Laser-induced graphene by multiple lasing: toward electronics on cloth, paper, and food [J]. ACS Nano, 2018, 12(3): 2176-2183.
- [23] Wang F C, Wang K D, Dong X, et al. Formation of hierarchical porous graphene films with defects using a nanosecond laser on polyimide sheet [J]. Applied Surface Science, 2017, 419: 893-900.
- [24] Ammar M R, Galy N, Rouzaud J N, et al. Characterizing various types of defects in nuclear graphite using Raman scattering: heat treatment, ion irradiation and polishing [J]. Carbon, 2015, 95: 364-373.
- [25] Malard L M, Pimenta M A, Dresselhaus G, et al. Raman spectroscopy in graphene [J]. Physics Reports, 2009, 473(5/6): 51-87.

Process Parameters of Direct Writing Polyimide by 1064 nm Fiber Laser

Wang Jin¹, Zhou Rudong³, Zhang Ning⁴, Cheng Junfeng¹, Cao Zheng¹, Wang Qiang¹,
Wu Dun^{1,5**}, Liu Chunlin^{1,2*}

¹ Jiangsu Key Laboratory of Environmentally Friendly Polymeric Materials, School of Materials Science and Engineering, Changzhou University, Changzhou, Jiangsu 213164, China;

² Changzhou University Huaide College, Jingjiang, Jiangsu 214500, China;

³ CNOOC Changzhou E.P. Coatings Co., Changzhou, Jiangsu 213016, China;

⁴ Changzhou Institute of Industry Technology, Changzhou, Jiangsu 213164, China;

⁵ Materials Science and Engineering National Experimental Teaching Demonstration Center,
Changzhou, Jiangsu 213164, China

Abstract

Objective In recent years, graphene-based nanomaterials have been widely studied because of their excellent chemical and physical properties. Among other applications, graphene has been successfully used in sensors and catalysis. Graphene can form a three-dimensional porous structure with a high surface area, depending on the method of synthesis. The assembly of graphene oxide (GO) into foam is one of the conventional methods employed to fabricate porous graphene structures. However, this approach needs the preparation of GO precursor via oxidative-acid synthesis route. Porous graphene can be processed via chemical vapor deposition on porous substrates, but high temperature and complex post-processing activities limit its commercialization. Recently, a facile approach to the formation and patterning of porous graphene on polyimide (PI) under ambient conditions using commercial laser scriber was reported. This one-step process of making laser-induced graphene is better than conventional methods for synthesizing porous graphene, and the method is also relatively simple and cheaper. Presently, there are few domestic studies on laser direct writing PI. In this present study, we report the effects of three sets of laser-process parameters on the carbon forming performance of 1064 nm laser direct writing PI films. We expect our methods and

findings to provide a reference for the process parameters of carbon forming of PI film written by 1064 nm laser.

Methods Commercial polyimide films were employed in experimental research. First, the 1064 nm fiber laser was used to directly write on the PI film, while the PI film carbonized after absorbing the laser energy. A scanning electron microscope, Raman spectrometer and X-ray photoelectron spectrometer were used to analyze the morphology and chemical composition of laser direct writing PI film. The four-probe and the contact angle measuring instruments were used to measure the conductivity and hydrophilicity of the laser direct writing PI film. The effects of three groups of parameters (spot size and line spacing; scanning speed and pulse frequency; laser power) on the carbon formation of PI film by laser direct writing were studied.

Results and Discussions The Raman spectrum shows that the laser direct writing PI film has three characteristic peaks of carbon: D peak at 1344 cm^{-1} , G peak near 1500 cm^{-1} , 2D peak at 2683 cm^{-1} (Fig. 3). The XPS results of the material show that there are C1s, O1s, and N1s peaks. Carbon atoms exist in four forms (C—C, C—O—C, C—N, and C=O), and the C—C bond is the main component of carbon (Fig. 4). The spot size, line spacing, scanning speed, and pulse frequency affect the conductivity of the laser direct writing PI film to certain degrees. When the laser power is low (1.8–2.0 W), the laser leaves some flocculation on the surface of the PI film. With an increase in laser power, holes gradually appear on the PI film, leading to the formation of a three-dimensional porous structure (Fig. 7). The contact angle of the laser direct writing PI film is positively correlated with the degree of damage of the PI film surface. By calculating the I_D/I_G and I_{2D}/I_G , it can be deduced that there is an initial decrease in the defect degree of the carbon layer, followed by an increase as the laser power increases (Fig. 8).

Conclusions In this study, using 1064 nm fiber laser direct writing PI film, the influence of laser-process parameters on PI film was studied. The PI film absorbs the pulse laser energy and performs a photothermal conversion, and finally forms a three-dimensional porous carbon layer. In the molecular chain of PI, chemical bonds such as C—H, C=O, C—N, etc. are broken and rearranged. The mass fractions of C, N, and O elements in the laser direct writing PI film are 84.84%, 2.02% and 13.14%, respectively. Using different laser processing-technology and parameters, the conductivity of the carbon layer formed by laser direct writing PI film is studied. The best combination of parameters for the conductivity of laser direct writing PI film was obtained: the laser line spacing was 0.001 mm, the spot size was 0.06 mm, the scanning speed was 150 mm/s and the pulse frequency was 40 kHz. With an increase in laser power, the degree of microscopic ablation morphology of the laser direct writing PI film gradually increases, and the surface changes from a small flocculent carbon particle to a three-dimensional porous carbon structure. With a laser power of 2.2 W, the carbon flaw is the lowest and the carbon crystallization rate is the highest. At this laser power, the sheet resistance is also the lowest ($55\text{ }\Omega/\text{sq}$). In addition, the contact angle of the laser direct writing PI film increases with a gradual increase in laser power. The surface of the laser direct writing PI film shows superhydrophobicity while the laser power is 2.8 W.

Key words laser technique; laser direct writing; polyimide; process parameters; carbonization performance

OCIS codes 140.3510; 160.5470; 310.3840